pH-INDUCED STRUCTURAL TRANSITIONS IN BSA HARD CORONA ON GOLD NANOPARTICLES MODULATE CURCUMIN LOADING AND RELEASE BEHAVIOR

M.P. SAMANT, V. JAISWAL, GAURI RAUT, P.M. DONGRE[#]

https://www.doi.org/10.59277/RJB.2026.2.01

[*]Department of Biophysics, University of Mumbai, Mumbai, India,
[#]e-mail: drpmdongre@yahoo.co.in

Abstract: The protein - nanoparticle corona structure directly determines nanoparticle stability, cellular uptake, and therapeutic outcome in biological media. In this study, we prepared a bovine serum albumin-gold nanoparticle hard corona (BSA-GNP HC) to examine the effects of pH on colloidal stability and curcumin binding. Dynamic light scattering and zeta potential measurements showed pH-dependent behavior governed by protein protonation at the nanoparticle surface. The corona remained stable at pH 7,6, and 2, with zeta potentials of –12.3 mV (pH 7) and +10.5 mV (pH 2), and a hydrodynamic diameter of about ~42 nm. At pH 4, near the BSA isoelectric point, the zeta potential was nearly zero (–1.04 mV), which produced strong aggregation and a particle size of ~846 nm; at pH 5, the size was about 69 nm, indicating partial destabilization. UV-Visible and fluorescence spectroscopy confirmed reversible structural changes between dispersed and aggregated states. Curcumin binding, quantified by fluorescence quenching, was measurable at pH 7 and 6, higher at pH 2, and not detectable at pH 4, where aggregation likely blocked binding sites. These data show that the BSA-GNP HC operates as a reversible supramolecular assembly controlled by protonation-dependent surface charge, suitable for pH-sensitive drug delivery in acidic environments.

Key words: Gold nanoparticles, protein corona, bovine serum albumin, hard corona, pH-responsive behavior, curcumin binding, drug delivery.

INTRODUCTION

In recent years, nanotechnology has emerged as a transformative field within biomedical research, largely due to the unique physicochemical properties exhibited by nanoparticles compared to their bulk material counterparts. When introduced into biological environments, nanoparticles readily interact with surrounding biomolecules such as proteins and lipids, leading to the spontaneous formation of an adsorbed biomolecular layer known as the protein corona [7, 36]. This corona can be broadly categorized into two components: a hard corona (HC), consisting of

Received: November, 2025;
in final form, May, 2026.

proteins tightly bound to the nanoparticle surface, and a soft corona (SC), formed by additional, more loosely associated protein layers [8, 24]. The presence of a protein corona alters the biological identity, stability, and cellular interactions of nanoparticles, often making their behavior markedly different from that of the uncoated particles.

These corona-mediated changes have been strategically utilized in targeted drug delivery, an approach designed to enhance therapeutic efficacy while minimizing off-target effects. Targeted delivery is particularly advantageous for drugs with poor solubility, limited stability, high systemic toxicity, or insufficient specificity [11]. Delivery strategies generally follow either passive or active targeting principles [9]. Passive targeting relies on the enhanced permeability and retention effect observed in tumor vasculature, which allows nanoparticles to accumulate preferentially in tumor tissues. In contrast, active targeting involves functionalizing the nanoparticle or corona with ligands that recognize and bind to receptors overexpressed on diseased cells, thereby promoting selective internalization [11, 38].

Metallic nanoparticles, particularly gold nanoparticles (GNPs), have gained considerable attention in this context. Their biocompatibility, tunable size, surface chemistry, and optical properties make them suitable for drug delivery and imaging applications [23]. Gold nanoparticles have been explored as drug delivery platforms in pancreatic cancer research, with growing interest in their therapeutic potential [50], while PEG functionalization is routinely used to enhance nanoparticle stability, extend blood circulation, and control cellular interactions [10]. Additionally, nanoparticle protein corona formation has been shown to modulate cytotoxicity and facilitate membrane transport [27, 32, 46]. In this study, gold nanoparticles (GNPs) were chosen because of their well-known optical stability and distinctive plasmonic properties [30]. Bovine serum albumin (BSA) was selected as a model protein due to its structural robustness and its well-documented ability to bind a wide range of molecules [39].

Nanoparticle protein corona systems intended for targeted drug delivery must navigate multiple biological environments, including the bloodstream, tumor microenvironment, intracellular compartments, and lysosomes [6]. Each of these environments presents distinct pH conditions: blood maintains a physiological pH of ~7.4, tumor tissues often exhibit a mildly acidic pH due to hypoxia and altered metabolism [44, 48], and lysosomes are strongly acidic. These variations can influence the structural integrity and functional behavior of the hard corona.

Therefore, in this study, we examined the stability and conformational state of the BSA-gold nanoparticle hard corona (BSA-GNP HC) under a range of pH conditions. In addition, we investigated the interaction of this corona with curcumin (CUR), a bioactive polyphenolic compound derived from *Curcuma longa*. The chemical structure of curcumin is shown in Fig. 1.

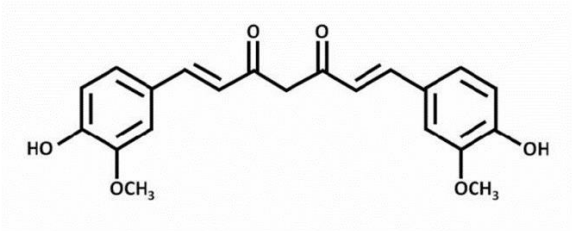

Fig. 1. Chemical structure of CUR. Adapted from Zhai *et al.* [51].

Curcumin (CUR) is widely recognized for its anticancer, antioxidant, anti-inflammatory, and anti-angiogenic activities. It has been shown to suppress tumor progression by down regulating anti-apoptotic pathways and enhancing the expression of tumor-suppressor genes such as p53 [1, 2, 15]. CUR also inhibits cancer cell proliferation by blocking NF-kappa B activation, reducing pro-inflammatory signaling, modulating STAT3 pathways, and promoting mitochondrial-mediated apoptosis through Bax activation and cytochrome-c release [31, 37, 45]. Numerous studies report the incorporation of CUR into nanocarrier systems to improve its stability and therapeutic efficacy, including CUR-functionalized silica nanoparticles [13] and polymeric or composite nanoformulations [29]. Based on this context, the present study examines the interaction of CUR with nanoengineered BSA-GNP hard corona across different pH conditions to assess pH-dependent binding behavior.

Although many studies have focused on identifying the composition of the protein corona, far fewer have examined how changes in environmental pH alter the structural arrangement of the hard corona and, in turn, influence its ability to bind therapeutic molecules. Understanding this relationship is crucial for the rational design of nanocarriers that can load and release drugs in a controlled, site-specific manner, particularly within physiological environments where pH varies significantly.

To address this gap, the present work explores how pH regulates the structural organization of a bovine serum albumin-gold nanoparticle hard corona and how these structural shifts affect the binding of curcumin. By integrating dynamic light scattering, zeta potential measurements, UV-Visible spectroscopy, and fluorescence quenching analysis, we demonstrate that changes in surface charge lead to reversible assembly and disassembly of the corona, which in turn determines the accessibility of ligand-binding sites.

These findings provide a clear mechanistic link between protonation-driven charge modulation, corona architecture, and drug binding efficiency. By demonstrating that the hard corona behaves as a dynamic and reversible structural entity, rather than a static coating, this work offers a conceptual foundation for

designing pH-responsive nanocarriers capable of tuning drug loading and release in accordance with local physiological conditions.

MATERIALS AND METHODS

Bovine serum albumin (BSA; Himedia), chloroauric acid ($HAuCl_4$; Molychem), trisodium citrate (Thomas Baker), and curcumin (Sigma-Aldrich) were used in this study. Buffer solutions of pH 2–7.4 were prepared using sodium phosphate monobasic (NaH_2PO_4), sodium phosphate dibasic ($Na_2HPO_4 \cdot 2H_2O$), and orthophosphoric acid (H_3PO_4). All chemicals and reagents were of analytical grade.

SYNTHESIS AND CHARACTERIZATION OF GOLD NANOPARTICLES (GNP)

Gold nanoparticles were synthesized using a standard chemical reduction approach following the procedure described by Pramanik *et al*. [41]. An aqueous solution of $HAuCl_4$ (0.25 mM) was heated to 95 °C under continuous stirring, after which trisodium citrate was added dropwise as the reducing and stabilizing agent. The gradual color transition of the solution served as a visual indicator of nanoparticle formation. The synthesized colloidal GNPs were characterized using UV-Visible spectroscopy to confirm their surface plasmon resonance, while scanning electron microscopy (SEM) coupled with energy dispersive spectroscopy (EDS) was employed to assess their morphology and elemental composition. Dynamic light scattering (DLS) and zeta potential measurements were further used to determine the hydrodynamic diameter and surface charge of the nanoparticles, respectively.

The nanoparticle concentration was calculated using Equation 1, as described previously (16).

$$C = \frac{N_{\mathrm{Total}}}{NV\mathrm{N_A}} \tag{1}$$

where N_{Total} is the total number of gold atoms added to the reaction mixture, N is the number of gold atoms present in each GNP ($N = 30.86 \times d^3$, d is the size of the GNP in nm), V is the volume of the solution in dm^3, and N_A is Avogadro's constant.

PREPARATION OF BSA-GNP HARD CORONA

Gold nanoparticles (0.074 nM) were incubated with increasing concentrations of BSA (0–45 μM) for 30 minutes to facilitate hard corona formation. Dynamic light scattering (DLS) was used to assess monolayer adsorption of BSA onto the nanoparticle surface, with all measurements performed in triplicate. Following

incubation, the mixture contained both BSA-GNP HC and unbound BSA. The hard corona complexes were isolated by centrifugation at 15,000 rpm for 10 minutes. The supernatant was carefully discarded, and the pellet was washed and resuspended in 10 mM buffer (pH 7.4). The purified BSA-GNP HC was then used for subsequent analyses.

CHARACTERIZATION TECHNIQUES

Dynamic light scattering (DLS) measurements

Dynamic light scattering was employed to determine the hydrodynamic diameter of BSA, GNP, and BSA-GNP hard corona (HC) samples under different pH conditions. Measurements were performed using a Zetasizer Nano ZS90 (Malvern Instruments) equipped with a 632.8 nm He-Ne laser, with scattered light detected at a fixed angle of 90 °. Refractive index of 1.33 and dispersant viscosity of 0.89 cP was set. Samples were equilibrated at 298 K in a 10 mm quartz cuvette, and each data point represents the average of three consecutive scans. DLS analysis was used to evaluate both the formation of the hard corona and the pH-dependent aggregation or dispersion behavior of the complexes. Changes in hydrodynamic size served as indicators of protein adsorption, corona restructuring, and nanoparticle assembly among varying pH environments.

Zeta potential measurements

Zeta potential analysis was conducted to assess surface charge and colloidal stability of BSA, GNP, and BSA-GNP HC across the pH range using the same instrument under identical environmental conditions. Measurements were performed in disposable folded capillary cells (DTS1070) to ensure reproducibility and minimize sample contamination. The zeta potential values were recorded in phosphate buffers of pH 2–7 to monitor protonation- and deprotonation-driven changes in charge distribution on the protein corona. These measurements provided insight into electrostatic repulsion or attraction between nanoparticles, helping to explain the observed transitions between stable dispersion, partial destabilization, and aggregation at specific pH values.

UV-Visible measurements

UV-Visible absorption measurements were performed to monitor the optical properties of BSA, GNP, and BSA-GNP hard corona (HC) under varying pH conditions. Spectra were recorded using a nanophotometer (Implen) in the wavelength range of 200–700 nm. BSA solutions (15 μM) and BSA-GNP HC samples were prepared in phosphate buffers adjusted to pH 2, 3, 4, 5, 6, and 7. All samples were analyzed in 10 mm pathlength quartz cuvettes at room temperature. For

GNP characterization, the characteristic surface plasmon resonance (SPR) band was used to confirm nanoparticle formation and assess any spectral shifts associated with protein adsorption. Changes in the absorbance profile of BSA across different pH conditions were used to evaluate possible pH-induced conformational variations in the protein. Similarly, shifts in the SPR band position or intensity in BSA-GNP HC samples were interpreted as indicators of corona formation, structural rearrangement, and pH-dependent aggregation state. All measurements were performed in triplicate, and representative spectra were used for comparative analysis.

Scanning electron microscope and energy dispersive spectroscopy

The morphology and elemental composition of the synthesized gold nanoparticles (GNPs) were characterized using a Nova NanoSEM (Model NPEP303). SEM imaging was conducted under high vacuum at an accelerating voltage of 15.00 kV, with a chamber pressure of 1.45×10^{-4} Pa. Images were acquired using a through-lens-detector (TLD) at a working distance of 5.3 mm and a spot size of 3.5, providing high-resolution surface topography at magnifications up to 100,000× (resolution ~500 nm; HEW = 4.14 µm). The SEM micrographs were used to assess particle morphology and uniformity. EDS analysis was performed to confirm the elemental composition of the nanoparticles and to exclude the presence of any unintended contaminants, such as residual chloride ions, trace metal contaminants from glassware or the reaction vessel, environmental metal particles, or instrumental artifacts. The spectrum showed only characteristic Au peaks, along with C and O signals from the citrate capping layer and Cu from the SEM chamber. Together, SEM and EDS data provided structural and compositional validation of the synthesized GNPs prior to protein corona formation.

Fluorescence spectroscopy measurements

Fluorescence measurements were carried out using a Varian Cary Eclipse spectrofluorometer to evaluate the conformational behavior of BSA and BSA-GNP HC across different pH conditions. Intrinsic fluorescence of BSA (1 mg/mL) was recorded at an excitation wavelength of 295 nm, and emission spectra were collected from 310–500 nm for samples prepared in buffers of pH 2–7. The excitation and emission slit widths were set to 10 nm. To assess the influence of nanoparticle binding on the protein microenvironment, fluorescence spectra of the BSA-GNP HC were recorded under the same pH conditions. The photomultiplier tube (PMT) voltage was adjusted (450 V for free BSA and 700 V for BSA-GNP HC) to account for scattering effects associated with nanoparticle presence.

Binding characteristic of BS-GNP HC with curcumin

The binding interaction between curcumin and the BSA-GNP hard corona was examined in selected buffer conditions (pH 7, 6, 4, and 2). Fluorescence

spectroscopy, due to its high sensitivity to microenvironmental changes around aromatic amino acids, was used to quantify the interaction. Fluorescence quenching data were analyzed to determine the Stern-Volmer quenching constant (K_{sv}) and the bimolecular quenching rate constant (K_q), providing insight into the quenching mechanism. Furthermore, the binding association constant (K_a) and the number of binding sites (n) were calculated to evaluate the strength and stoichiometry of CUR binding to the corona. For fluorescence measurements, intrinsic tryptophan residues of BSA within the corona were selectively excited at 295 nm, and emission spectra were recorded from 310-500 nm. The excitation and emission slit widths were maintained at 10 nm, and the photomultiplier tube (PMT) voltage was set to 700 V to ensure optimal signal detection in nanoparticle-containing samples.

RESULT AND DISCUSSION

The formation of gold nanoparticles (GNPs) was initially indicated by a distinct color change of the reaction mixture from pale yellow to ruby red, characteristic of nanoparticle formation. UV-Visible spectroscopy confirmed this observation, showing a prominent surface plasmon resonance (SPR) peak at approximately 520 nm (Fig. 2b), which reflects the collective oscillation of conduction electrons at the nanoparticle solvent interface. The position and shape of this SPR band are sensitive to changes in the surrounding dielectric environment. Therefore, adsorption of bovine serum albumin onto the GNP surface is expected to induce a measurable red shift in the absorption peak due to alterations in local refractive index. In Fig. 2a, the dynamic light scattering measurements revealed that the synthesized GNPs had an average hydrodynamic diameter of 28.87 ± 1 nm. Using established calculations (Eq. 1), the nanoparticle concentration was determined to be 0.37 nM.

To determine the saturation point of protein adsorption on the nanoparticle surface, GNPs (0.074 nM) were incubated with increasing concentrations of BSA ranging from 0 to 45 μM. Dynamic light scattering analysis showed a progressive increase in hydrodynamic diameter with rising BSA concentration, indicating the stepwise formation of the protein corona (Fig. 2c). After centrifugation to isolate the hard corona, a further slight increase in particle size was observed, confirming the formation of a stably bound protein layer.

At a BSA concentration of 15 μM, the BSA-GNP corona measured 35.9 ± 1 nm, while the corresponding hard corona exhibited a hydrodynamic diameter of 38.32 ± 2 nm. Considering the molecular dimensions of BSA, an increase of approximately 10 nm in particle size is consistent with monolayer adsorption of BSA molecules onto the GNP surface, likely in an end-on orientation [47]. Assuming an end-on orientation of BSA, based on its reported molecular

dimensions (~4 × 4 × 14 nm) [39], the corresponding molecular footprint is approximately 16 nm². Using a geometric monolayer coverage approach as described by Röcker *et al*. [43], the estimated maximum surface coverage corresponds to approximately 144 BSA molecules per nanoparticle.

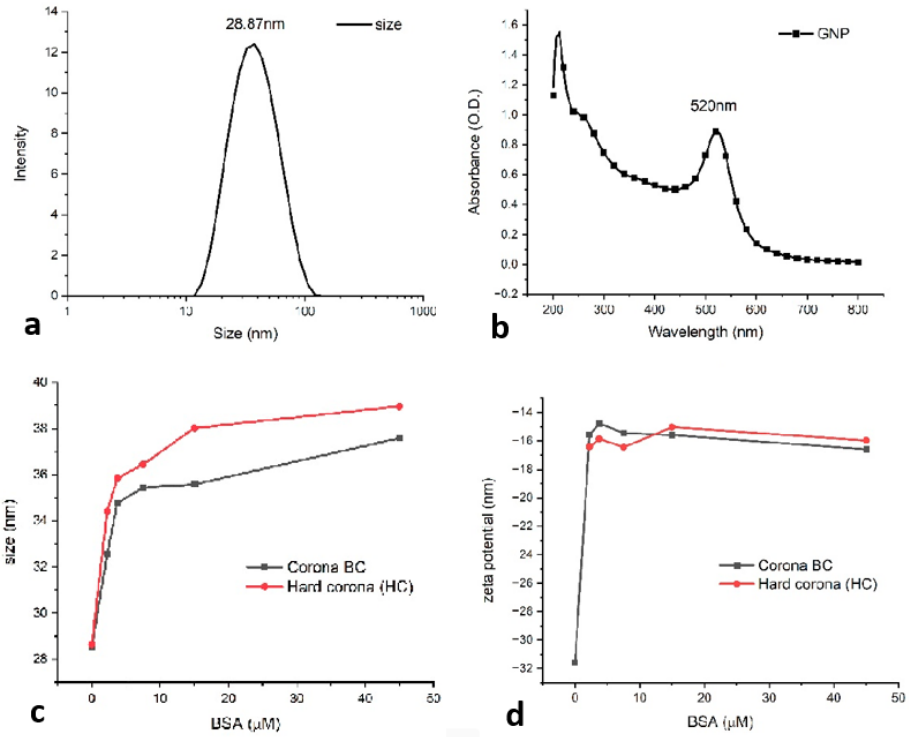

Fig. 2. a) UV-Visible spectrum (top right) and b) DLS (top left) of synthesized GNP, c) is DLS (bottom left) and d) is zeta potential (bottom right) of corona before centrifugation (corona BC) and HC.

The zeta potential of the synthesized GNPs was measured to evaluate their surface charge and colloidal stability. The nanoparticles exhibited a zeta potential of –31.9 mV, indicating a relatively high negative surface charge. Zeta potential reflects the electrostatic potential at the slipping plane of particles in suspension and is widely used to predict nanoparticle stability in aqueous media. In general, nanoparticles with zeta potential values greater than ±30 mV are considered electrostatically stable due to sufficient repulsive forces that prevent aggregation [12]. Following the adsorption of BSA onto the GNP surface, a decrease in the magnitude of the zeta potential was observed. This reduction is consistent with partial charge neutralization upon protein adsorption, confirming successful corona

formation. Similar trends have been reported previously, where protein binding to GNPs results in decreased zeta potential values [12, 18]. The zeta potential profiles of the BSA-GNP hard corona (HC) complexes are shown in Fig. 2d. Based on the size and charge behavior, the HC prepared using 15 μM BSA and 0.074 nM GNP corresponding to monolayer coverage was selected for subsequent experiments.

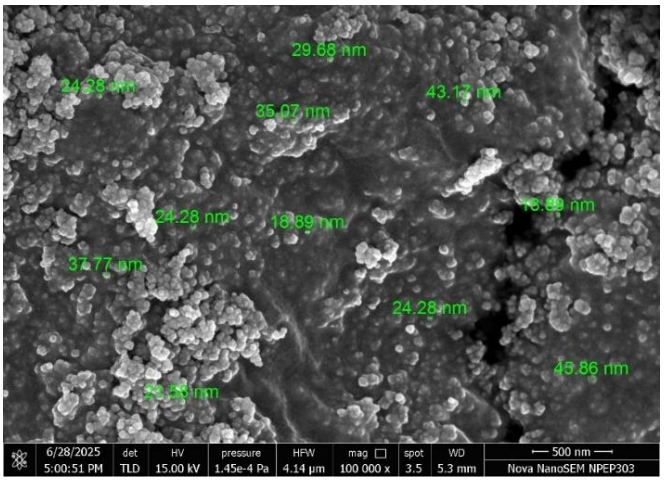

Fig. 3. Scanning electron microscope (SEM) image of GNP.

SEM image in Fig. 3 revealed that the synthesized gold nanoparticles were predominantly spherical and well dispersed, with no evidence of large-scale aggregation. The particle surfaces appeared smooth and uniform, indicating stable citrate capping during synthesis. The size of particles seen were in range of 18–45 nm as shown in Fig. 3.

To obtain a statistically reliable representation of the particle size distribution, SEM micrographs were quantitatively analyzed using a custom Python-based image-processing workflow. A total of 1065 individual nanoparticles were measured, providing a robust dataset for statistical evaluation. The extracted particle diameters yielded a mean size of 34.41 nm with a standard deviation of 17.55 nm. Based on these values, the nanoparticle polydispersity index ($PDI = \sigma/\mu$) was calculated to be 0.51, indicating a broad size distribution within the synthesized sample.

Most particles were distributed within the 18–50 nm range, with the highest frequency observed in the 18.2–21.5 nm bin (279 particles), suggesting a predominance of smaller nanoparticles. However, the distribution was not symmetric and exhibited a noticeable tail toward larger diameters. To better describe this asymmetry, the probability density data were fitted using a log-normal model, which provided an excellent fit ($R^2 = 0.97$), confirming that the size

distribution follows a positively skewed pattern rather than a symmetric Gaussian profile.

Such log-normal behavior is consistent with size-dependent growth kinetics in citrate-mediated gold nanoparticle synthesis. SEM images further confirm that the nanoparticles are predominantly spherical, with the observed polydispersity arising mainly from growth heterogeneity.

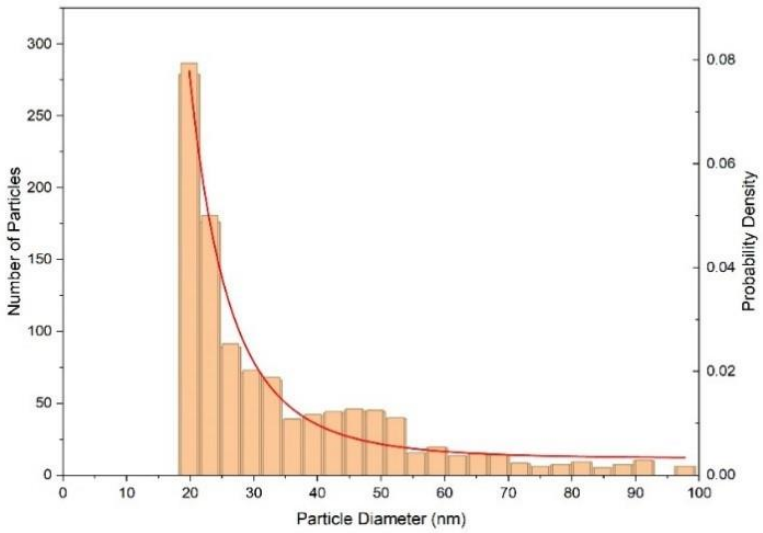

Fig. 4. Particle distribution analysis of the SEM image of spherical particles.

.

Figure 5 EDS spectrum exhibited a strong characteristic Au M_α peak at approximately 2.12 keV, confirming the presence of metallic gold. A weaker Au L_α peak near 9.7 keV was also observed, consistent with the expected emission profile for gold nanoparticles at an accelerating voltage of 15 kV.

The spectrum showed a predominant signal for gold (Au), contributing 57.89 % of the normalized elemental weight composition, confirming the presence of metallic gold as the major constituent. In addition, signals corresponding to carbon (31.08 %) and oxygen (9.81 %) were detected. These elements are commonly observed in citrate-stabilized nanoparticles and may also arise from the carbon-based SEM sample support and adsorbed atmospheric species. The low-intensity peaks at ~4.8, ~5.3, and ~5.7 keV arise from Kα emissions of transition-metal components (primarily Cr, V, and Mn) in the SEM chamber and stage hardware, and not from the Au nanoparticles themselves. The Au M-lines were observed at ~2.12–2.20 keV as expected. Overall, the strong Au peak and characteristic elemental profile confirm successful synthesis of gold nanoparticles with citrate-based surface stabilization.

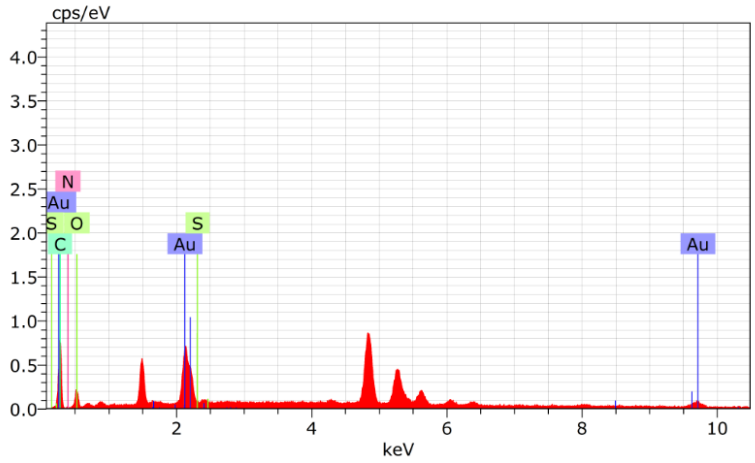

Fig. 5. Energy dispersive spectroscopy of GNP.

EFFECT OF PH ON BSA AND BSA-GNP HC

UV-Visible spectroscopy study

Studies have shown that the net charge of BSA is strongly dependent on the pH of the surrounding medium [39]. When the zeta potential approaches zero, the protein attains a near-neutral net charge, corresponding to conditions close to its isoelectric point [12, 49]. As the pH approaches the isoelectric point, the electrostatic repulsion between BSA molecules decreases, which may reduce the stability of their adsorption on the nanoparticle surface [39]. In addition, the surface chemistry of gold nanoparticles is known to be influenced by changes in pH; therefore, direct interaction between the buffer components and the exposed GNP surface could promote particle-particle association, contributing to aggregation [28].

The UV-Visible spectra in Fig. 6 and Fig. 7 showed a clear pH-dependent structural response for both BSA and the BSA-GNP hard corona (HC). Native BSA exhibited characteristic absorption peaks at approximately 230 nm and 280 nm at pH 7, which correspond to peptide bond transitions and the presence of aromatic amino acids such as tryptophan and tyrosine, respectively. These absorptions arise from π-π^* electronic transitions within the aromatic rings [4,40]. When the pH was lowered to 6 and 5, these peaks remained visible but displayed a hyperchromic shift, suggesting minor conformational rearrangements in the protein due to partial protonation of surface residues. At a more acidic pH (<4), BSA showed an increased absorbance at 280 nm, indicating partial unfolding and increased exposure of aromatic residues to the solvent environment [42].

The relative absorbance values at 280 nm and 520 nm provide clear evidence of the pH-dependent stability of the BSA-GNP hard corona system. Changes were observed not only in intensity but also in the position of the SPR band. At pH 7 and 6, the SPR maximum remained centered at 520 nm with moderate intensity (0.19895 a.u.), indicating a stable and well-dispersed corona-coated nanoparticle system.

As the pH decreased to 5, the SPR band shifted to 546 nm and showed increased intensity (0.38953 a.u.), reflecting changes in the surrounding dielectric environment and enhanced interparticle interactions. At pH 4, the SPR peak shifted slightly to 537 nm, but its intensity dropped markedly (0.12815 a.u.), signaling pronounced aggregation near the isoelectric region of BSA, where electrostatic stabilization is weakest.

Further lowering the pH to 3 resulted in the SPR band reappearing at 546 nm with intermediate intensity (0.38953 a.u.), suggesting partial stabilization. At pH 2, however, the peak shifted back toward 521 nm and displayed the highest intensity (0.61838 a.u.), indicating redispersion of the nanoparticles under strongly acidic conditions. This shift back toward shorter wavelengths supports restoration of electrostatic repulsion due to increased positive surface charge.

A similar pH-dependent pattern was observed at 280 nm, corresponding to absorption by aromatic residues of BSA. The lowest intensity again occurred at pH 4 (0.18431 a.u.), while higher values were recorded at pH 2 (0.60722 a.u.) and intermediate values at pH 3 and 5 (0.33044 a.u.), with moderate intensities at pH 6 and 7 (0.22 a.u.). Also, the spectral changes were reflected visually, as the dispersion shifted from ruby red at neutral pH 7 to pale or whitish near pH 4, before returning toward red at pH 2.

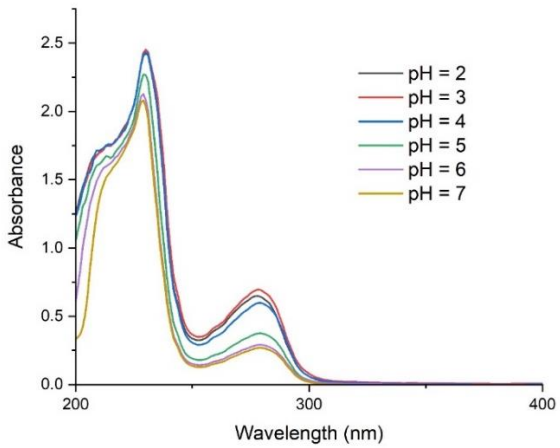

Fig. 6. UV-Visible spectra of BSA in different pH.

Such visual behavior and simultaneous decrease at both wavelengths around pH 4 likely results from aggregation and temporary destabilization of the hard corona near the isoelectric point, potentially exposing portions of the nanoparticle surface to the surrounding medium.

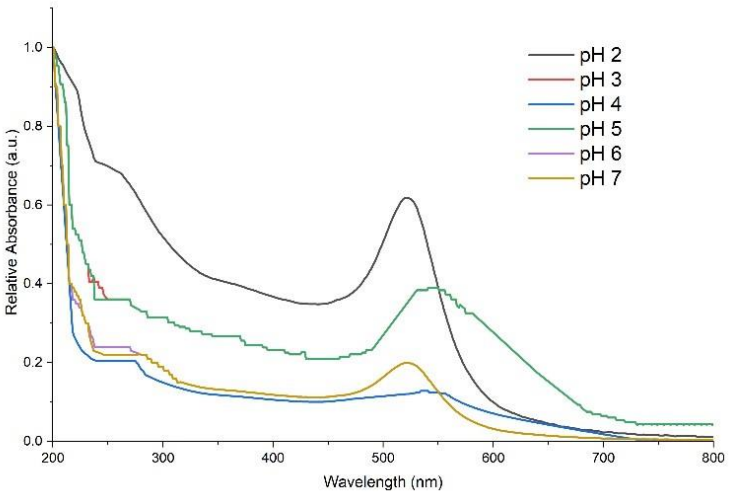

Fig. 7. UV-Visible spectra of BSA-GNP HC in different pH.

At pH 2, BSA carries a net positive charge, which reintroduces electrostatic repulsion between individual BSA-GNP HC complexes. Consequently, the dispersion regains stability, restoring both the solution color and the SPR signal intensity at 520 nm (Fig. 6). This re-stabilization is consistent with trends observed in the DLS and zeta potential measurements presented in the following section.

Collectively, these observations indicate that the hard corona effectively protects the gold nanoparticle core at pH 7, 6, 5, and 2. However, at pH 4, where the zeta potential approaches neutrality, the system becomes destabilized, resulting in pronounced aggregation. A similar behavior is also evident at pH 3, supporting the central role of electrostatic charge in maintaining corona integrity (Fig. 7). Overall, the results underscore the crucial role of pH-driven surface charge modulation in maintaining protein corona integrity and nanoparticle stability.

Dynamic light scattering study

To further evaluate the aggregation state of the BSA-GNP HC under varying pH conditions, DLS measurements were conducted using the same instrumental parameters applied during initial nanoparticle characterization. The hydrodynamic size data are summarized in Table no 1 and represented in Fig. 8.

At pH 7 and pH 6, the BSA-GNP HC displayed average diameters of 42.02 ± 2 nm and 41.66 ± 2 nm, respectively, indicating a compact and stable corona structure. A similar stability was observed at pH 2, where the average diameter was 43.69 ± 2 nm.

In these conditions, the complexes maintain sufficient surface charge negative at pH 7 and 6, and positive at pH 2 leading to effective electrostatic repulsion that prevents aggregation. At pH 5, the hydrodynamic diameter increased to 68.73 nm, suggesting the onset of partial clustering due to a decrease in net surface charge. This trend became much more pronounced near the isoelectric region of BSA. At pH 4 and pH 3, a dramatic increase in particle size was recorded, with the most substantial aggregation observed at pH 4, where the hydrodynamic diameter reached 846 ± 5 nm.

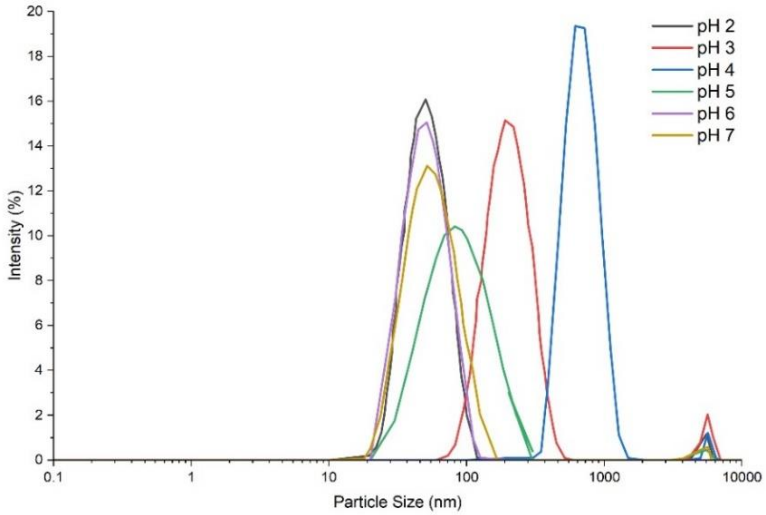

Fig. 8. Dynamic light scattering of BSA-GNP HC in different pH.

This coincided with the zeta potential approaching zero, a condition under which electrostatic repulsion is minimized and attractive forces dominate. The visible color change to a pale purple at pH 4 further corroborates the formation of large aggregated assemblies.

These findings are in strong agreement with the UV-Visible spectral trends and confirm that the aggregation observed near pH 4 results from charge neutralization and structural rearrangement within the BSA corona, rather than instability of the gold core itself. In contrast, at very low pH (pH 2), the positive charge acquired by BSA restores repulsive interactions, enabling the disassembly of aggregates and re-establishing a stable, dispersed HC structure.

Table no 1

Z average size of the BSA-GNP HC at various pH

pH	Average size (*d*) (nm)
2	43.69 ± 2
3	204 ± 3
4	846 ± 5
5	68.73 ± 2
6	41.66 ± 2
7	42.02 ± 2

Zeta potential study

Zeta potential provides information about the electrical potential at the slipping plane between a particle's surface and the surrounding medium and is therefore a useful indicator of both colloidal stability and surface charge characteristics [12]. In the present study, zeta potential measurements were recorded for BSA and BSA-GNP HC across a pH range of 2–7 (Fig. 9). As expected, the surface charge of BSA shifted systematically with pH. At higher pH values, BSA carried a net negative charge due to deprotonation of acidic residues. When the pH approached the isoelectric point, the net charge decreased, and at pH 4 the zeta potential approached 0 mV. At lower pH values, protonation of ionizable amino acid side chains resulted in a net positive charge [12, 19, 39]. Specifically, BSA exhibited a zeta potential of –9.9 mV at pH 7, indicating negatively charged, moderately stable protein dispersions. At pH 2, the zeta potential shifted to +9.21 mV, reflecting a reversal of surface charge and re-establishment of electrostatic repulsion, which helps maintain dispersion stability. In contrast, at intermediate pH values (pH 3, 5, and 6), reduced magnitude of surface charge corresponded with decreased stability. Extrapolation of the zeta potential profile indicated that the isoelectric point occurs near pH 4.

A similar pH-dependent trend was observed for the BSA-GNP hard corona. At pH 7 and pH 2, the BSA-GNP HC displayed zeta potential values of –12.3 mV and +10.5 mV, respectively, consistent with stable, dispersed complexes. However, at pH 4, the zeta potential of the BSA-GNP HC decreased to –1.04 mV, effectively close to zero and approaching charge neutrality. Extrapolation placed the effective isoelectric point of the HC near pH 3.8. This significant shift in the charge profile compared to free BSA reflects the adsorption of BSA onto the GNP surface and subsequent rearrangement of surface-exposed ionizable groups [32, 46]. Because electrostatic repulsion is minimized at this condition, aggregation is supported by

the increase in hydrodynamic diameter observed in DLS and by the notable reduction in intensity and broadening of the SPR band at ~520 nm in the UV-Visible spectra. Taken together, the zeta potential results confirm that surface charge modulation is the key regulator of BSA-GNP HC stability, with aggregation occurring specifically when the system approaches charge neutrality.

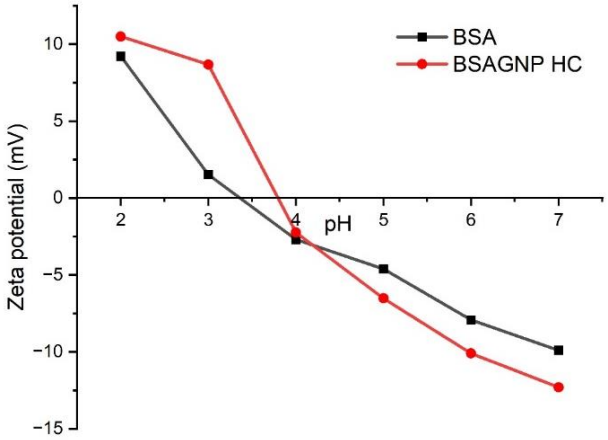

Fig. 9. Zeta potential of BSA and BSA-GNP corona in pH 2–7.

Fluorescence spectroscopy study

Fluorescence spectroscopy was employed to examine pH-dependent conformational changes in BSA and to understand how these structural changes are altered when BSA is adsorbed onto the gold nanoparticle surface. Since excitation at 295 nm selectively excites tryptophan residues, the resulting emission spectra provide a sensitive probe of the microenvironment surrounding tryptophan and, in turn, reflect the conformational state of the protein. At physiological pH, native BSA displayed a characteristic emission maximum at approximately 344 nm (Fig. 10), which corresponds to tryptophan residing in a moderate polar environment within the protein core [25]. A similar emission wavelength was observed at pH 7, indicating that the tertiary structure of BSA remains largely intact.

As the pH decreased to 6 and 5, an increase in fluorescence intensity was observed, accompanied by a blue shift of approximately 2–3 nm relative to pH 7. These spectral changes suggest a subtle tightening of the tertiary structure or reduced solvent exposure of tryptophan residues. Such effects are consistent with small conformational rearrangements driven by partial protonation of surface residues. At pH 4, however, the fluorescence intensity decreased relative to values at pH 5, 6, and 7, while the emission maximum was recorded near 343 nm. This

decrease in intensity indicates that BSA undergoes partial unfolding or loosening of its tertiary structure when approaching its isoelectric point, where reduced electrostatic repulsion promotes conformational rearrangements [5].

Below the isoelectric region, more substantial spectral changes were observed. At pH 3, the fluorescence intensity increased markedly, and the emission maximum shifted by ~9 nm toward the blue region compared to pH 7. This indicates significant rearrangement within the protein, potentially involving exposure of hydrophobic residues or repositioning of tryptophan into a less polar microenvironment. At pH 2, fluorescence was highly quenched and the emission maximum remained ~9 nm blue shifted. Strong quenching at low pH may result from large-scale unfolding, increased solvent exposure, and enhanced non-radiative decay processes [14, 26]. These findings are consistent with earlier reports showing that pH-dependent protonation and deprotonation of amino acid residues influence protein structural stability, the spatial arrangement of aromatic residues, and their fluorescent behavior [5]. Moreover, changes in electrostatic interactions and the local charge environment also contributed to fluorescence quenching and decreased emission intensity [3].

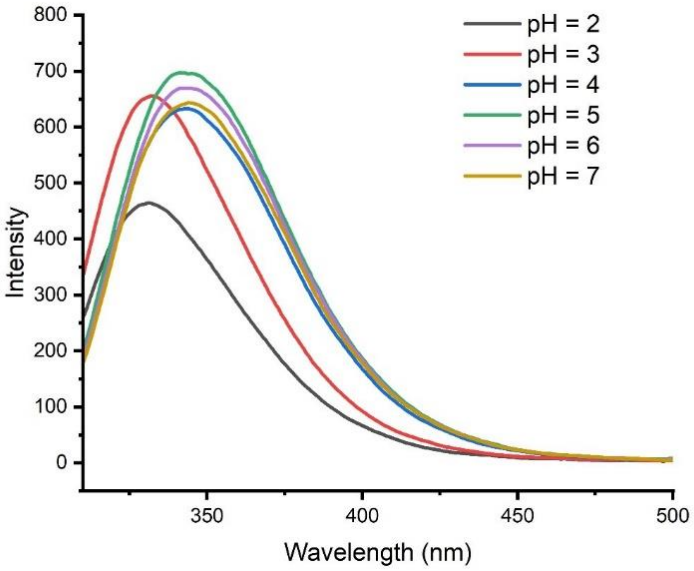

Fig. 10. Fluorescence Spectra of BSA in different pH.

The fluorescence spectra of the BSA-GNP hard corona showed pH-dependent behavior similar to free BSA, with distinct differences upon nanoparticle binding. At pH 7, the emission maximum shifted to ~328 nm (Fig. 11), indicating a blue shift

relative to native BSA. This shift suggests reduced solvent exposure and a more hydrophobic microenvironment around tryptophan residues following adsorption [21, 34]. The fluorescence intensity decreased, indicating nanoparticle-induced quenching caused by close proximity to the gold surface, independent of the blue shift. Across pH 6 and 5, the fluorescence intensity increased (similar to free BSA), suggesting tighter packing or reduced solvent access around tryptophan. When the pH was reduced to 4, 3, and 2, the fluorescence intensity gradually decreased again. Previous studies have shown that protonation near the isoelectric point of BSA leads to partial conformational loosening and increased hydrophobic residue exposure, which correlates with the decreased emission intensity observed [22]. Additionally, pH fluctuations are known to disrupt and reform hydrogen bonding networks within proteins, affecting tertiary stabilization and fluorophore quencher distances [3, 14, 25].

However, the fluorescence spectra did not provide clear evidence for BSA desorption from the GNP surface near the isoelectric point. While aggregation and corona restructuring were evident from UV-Visible and DLS analyses, the fluorescence behavior remained consistent with BSA largely remaining associated with the gold surface. Thus, fluorescence results support that pH primarily affects the conformation and packing of adsorbed BSA, rather than causing complete desorption.

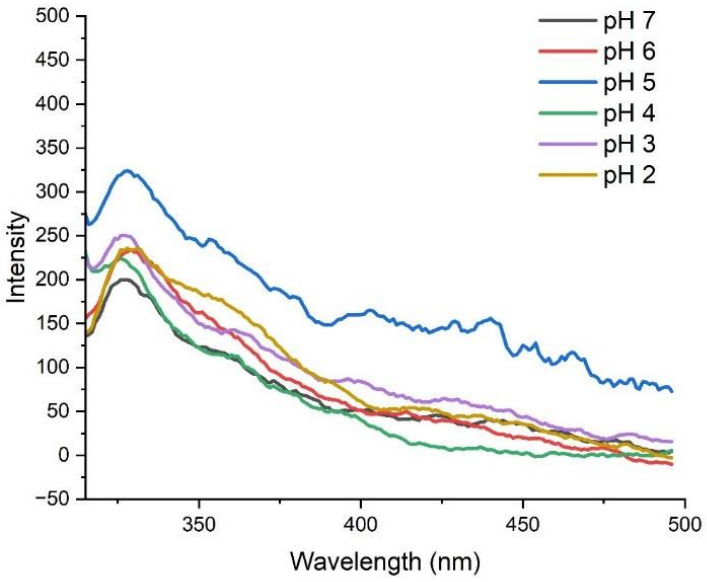

Fig. 11. Fluorescence spectra of BSA-GNP HC in different pH.

INTERACTION OF BSA-GNP HARD CORONA WITH CURCUMIN

Fluorescence spectroscopy study

The fluorescence spectra of BSA-GNP HC and CUR interaction is shown in Fig. 12. a decrease in fluorescence intensity was observed upon CUR addition, indicating quenching of BSA-GNP HC fluorescence. Similar quenching behavior of BSA upon interaction with CUR has been reported previously [17, 35]. Fluorescence quenching is the process in which the fluorescence intensity of a given fluorophore decreases. Molecular interactions between the BSA and CUR generate the quenching effect. Quenching phenomenon could be the result of collisional quenching (dynamic quenching) or non-fluorescent ground state complex formation (static quenching). Dynamic (collisional) quenching is a process where fluorophore in its excited state collides with the quencher molecule; whereas in static quenching non-fluorescent conjugate between the fluorophore and the quencher is formed in the ground state [25].

Stern-Volmer equation (equation 2) was used to calculate the Stern-Volmer constant K_{sv} which represent the efficiency of the quenching, i.e., it indicates the accessibility of the quencher to the excited fluorophore.

$$\frac{F_0}{F} = 1 + k_q\tau_0[Q] = 1 + K_{\mathrm{SV}}[Q] \quad (2)$$

$$K_{\mathrm{SV}} = k_q\tau_0 \quad (3)$$

where [Q] is the concentration of quencher. F_0 and F are the fluorescence intensities of BSA in absence and presence of quencher, respectively. k_q is the biomolecular quenching rate constant and τ_0 is the lifetime of biopolymer (10–8 s) without quencher [25].

Binding constant (K) of CUR and BSA-GNP HC interaction and number of binding site (binding number, n) of CUR on BSA was calculated using double logarithmic equation (Eq. 4).

$$\log\frac{F_0-F}{F} = \log K + n\log[Q] \quad (4)$$

The fluorescence emission spectra illustrating the interaction between the BSA-GNP hard corona (HC) and curcumin (CUR) at pH 7, 6, 4, and 2 are shown in Fig. 12. The BSA-GNP HC displays an emission maximum at approximately 322 nm, consistent with quenching of tryptophan fluorescence in the presence of the gold nanoparticle surface.

Upon titration with increasing concentrations of CUR, a progressive decrease in fluorescence intensity was observed, indicating that CUR interacts with the protein corona in a manner that alters the microenvironment surrounding the fluorophore. This quenching behavior aligns with our previous observations on

CUR interacting with nanoparticle-protein corona complexes [20]. To further understand the quenching mechanism and binding strength, Stern-Volmer and double logarithmic analyses were performed. The calculated Stern-Volmer quenching constants (K_{sv}), bimolecular quenching constants (K_q), association constants (K_a), and number of binding sites (n) are summarized in Table 2.

At pH 7, the BSA-GNP HC displayed a K_{sv} value of 1.99×10^4 M^{-1} and a K_q value of 3.98×10^{12} $M^{-1}s^{-1}$. At pH 6, the K_{sv} and K_q values were 1.81×10^4 M^{-1} and 3.62×10^{12} $M^{-1}s^{-1}$, respectively. These K_q values are significantly higher than the typical diffusion-controlled limit (~10^{10} $M^{-1}s^{-1}$), indicating that the quenching arises from static quenching, which reflects ground-state complex formation rather than collisional interactions [25, 33]. The association constants (K_a) at pH 7 and 6 (1.81×10^2 M^{-1} and 1.019×10^2 M^{-1}, respectively), along with n values below 1 (0.58 at pH 7 and 0.54 at pH 6), suggest that CUR interacts with a single dominant binding site on the BSA-GNP HC under these conditions.

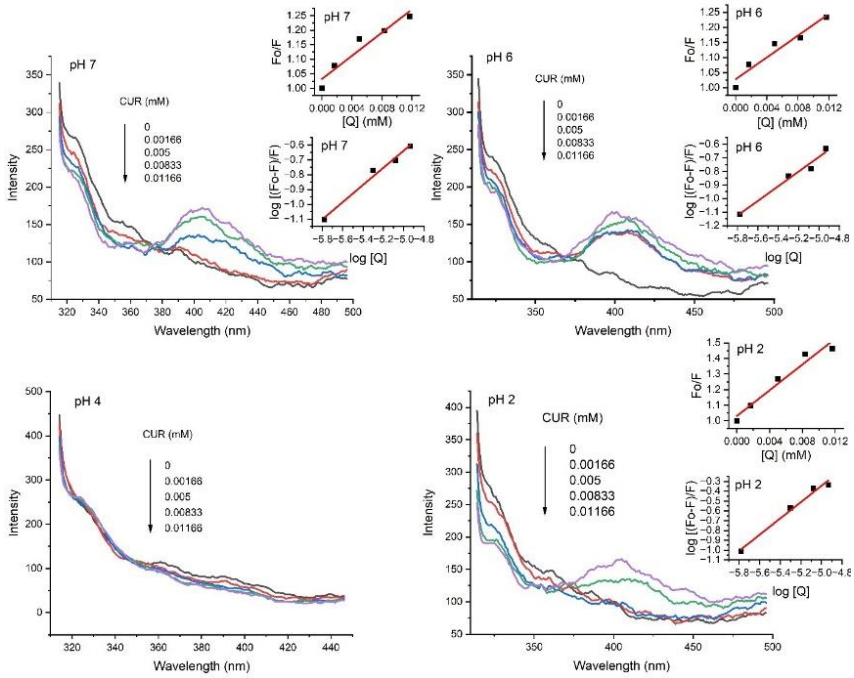

Fig. 12. Fluorescence spectra of interaction between BSA-GNP HC and CUR for pH 7, 6, 4, and 2. Stern-Volmer plot and double logarithmic plots for pH 7, 6, and 2 are shown in inset.

Notably, at pH 2, the binding affinity increased substantially. The K_{sv} rose to 4.13×10^4 M^{-1}, K_q to 8.26×10^{12} $M^{-1}s^{-1}$, and K_a to 6.51×10^3 M^{-1}, with $n = 0.83$. The enhanced binding at pH 2 corresponds to the positively charged and

re-stabilized state of the corona, which likely increases the accessibility of CUR-binding residues.

In contrast, at pH 4, no appreciable quenching was observed, and no binding parameters could be calculated. This absence of interaction correlates directly with the extensive aggregation observed in DLS and UV-Visible analyses at pH 4, where the corona collapses due to charge neutralization near the isoelectric point. In this aggregated state, binding sites are sterically shielded and unavailable for CUR interaction.

Table 2

Stern-Volmer constant (K_{sv}), quenching constant (K_q), association constant (K_a) and number of bindings sites (n) of BSA-GNP HC conjugate at various pH 2, 4, 6, and 7

pH of BSA-GNP HC	K_{sv} (M^{-1})	K_q ($M^{-1}s^{-1}$)	n	K_a (M^{-1})
pH 7	1.99×10^4	3.98×10^{12}	0.58	1.81×10^2
pH 6	1.81×10^4	3.62×10^{12}	0.54	1.019×10^2
pH 4	–	–	–	–
pH 2	4.13×10^4	8.26×10^{12}	0.83	6.51×10^3

Taken together, these data demonstrate that CUR binding to the BSA-GNP HC is strongly governed by the pH-dependent structural state of the corona. When the corona is dispersed (pH 7, 6, and 2), CUR can associate effectively; however, when the corona aggregates (pH 4), ligand binding is inhibited. This confirms that corona assembly-disassembly dynamics directly control drug accessibility, highlighting the relevance of pH-responsive nanostructures in drug delivery applications.

CONCLUSION

This study provides a comprehensive understanding of how pH influences the structural stability and functional behavior of the BSA-GNP hard corona. UV-Visible spectroscopy revealed distinct spectral changes associated with pH-driven aggregation and disassembly of the corona, particularly the disappearance and reappearance of the gold nanoparticle plasmon band near the isoelectric region. DLS measurements confirmed these observations, showing that the corona remains compact and stable at pH 7, 6, and 2 (hydrodynamic diameter ~42 nm), undergoes partial destabilization at pH 5 (~68.73 nm), and exhibits extensive aggregation at

pH 4 (846 ± 5 nm). Zeta potential analysis further established that this behavior is governed by protonation-dependent surface charge regulation; the corona is stable when sufficiently charged (–12.3 mV at pH 7 and +10.5 mV at pH 2) and aggregates when the charge approaches neutrality at pH ~4.

Fluorescence spectroscopy of both free BSA and BSA-GNP HC demonstrated pH-sensitive conformational changes within the protein shell, reflecting alterations in the microenvironment of tryptophan residues during corona compaction and expansion. Curcumin binding studies revealed static quenching and ground-state complex formation at pH 7, 6, and 2, indicating accessible binding sites under dispersed conditions. In contrast, no appreciable binding was observed at pH 4, where corona aggregation restricts ligand accessibility.

Taken together, these findings show that the BSA-GNP hard corona is not a rigid surface layer but a dynamic, reversible supramolecular assembly whose structural state and functional ligand binding capacity are determined by environmental pH. The reversible aggregation at pH 4 and redispersion at pH 2 highlights the plasticity of the corona architecture. This pH-responsive behavior has significant implications for nano drug delivery design, suggesting that drug loading and release can be strategically tuned by exploiting pH variations across physiological and pathological environments.

Acknowledgements. The authors are grateful to the Department of Biophysics, University of Mumbai for their support.

Competing interest: The authors declare that they have no competing interests.

Declaration of generative AI and AI-assisted technologies in the writing process: During the preparation of this work the author used AI-assisted tools (*e.g.*, QUILBOT) for language editing and grammar correction. The scientific content, analysis, and conclusions are entirely the responsibility of the author.

REFERENCES

1. AGGARWAL, B.B., W. YUAN, S. LI, S.C. GUPTA, Curcumin-free turmeric exhibits anti-inflammatory and anticancer activities: Identification of novel components of turmeric, *Molecular Nutrition & Food Research*, 2013, **57**(9), 1529–1542, https://doi.org/10.1002/mnfr.201200838.
2. ANAND, P., A.B. KUNNUMAKKARA, R.A. NEWMAN, B.B. AGGARWAL, Bioavailability of curcumin: problems and promises, *Molecular Pharmaceutics*, 2007, **4**(6), 807–818, https://doi.org/10.1021/mp700113r.
3. BALER, K., O.A. MARTIN, M.A. CARIGNANO, G.A. AMEER, J.A. VILA, I. SZLEIFER, Electrostatic unfolding and interactions of albumin driven by pH changes: A molecular dynamics study, *Journal of Physical Chemistry B*, 2014, **118**(4), 921–930, https://doi.org/10.1021/jp409936v.
4. BERG, J.M., J.L. TYMOCZKO, L. STRYER, *Biochemistry*, W.H. Freeman, 2002.
5. BHATTACHARYA, M., N. JAIN, K. BHASNE, V. KUMARI, S. MUKHOPADHYAY, pH-Induced conformational isomerization of bovine serum albumin studied by extrinsic and

intrinsic protein fluorescence, *Journal of fluorescence*, 2011, **21**(3), 1083–1090, https://doi.org/10.1007/s10895-010-0781-3.

6. BLANCO, E., H. SHEN, M. FERRARI, Principles of nanoparticle design for overcoming biological barriers to drug delivery, *Nature Biotechnology*, 2015, **33**(9), 941–951, https://doi.org/10.1038/nbt.3330.
7. CEDERVALL, T., I. LYNCH, S. LINDMAN, T. BERGGÅRD, E. THULIN, H. NILSSON, KENNETH A. DAWSON S. LINSE, Understanding the nanoparticle-protein corona using methods to quantify exchange rates and affinities of proteins for nanoparticles, 2007, *PNAS*, **107**(4), 2050–2055, www.pnas.org/cgi/content/full/.
8. CHAKRABORTY, D, K.R. ETHIRAJ, A. MUKHERJEE, Understanding the relevance of protein corona in nanoparticle-based therapeutics and diagnostics, *RSC Advances*, 2020, **10**(45), 27161–27172, https://doi.org/10.1039/d0ra05241h.
9. DAVIS, M.E., Z.G. CHEN, D.M. SHIN, Nanoparticle therapeutics: an emerging treatment modality for cancer, *Nature Reviews Drug Discovery*, 2008, **7**(9), 771–782, https://doi.org/10.1038/nrd2614.
10. EL-BAZ, N, B.M. NUNN, P.J. BATES, M.G. O'TOOLE, The impact of PEGylation on cellular uptake and *in vivo* biodistribution of gold nanoparticle MRI contrast agents, *Bioengineering*, 2022, **9**(12), 766, https://doi.org/10.3390/bioengineering9120766.
11. FAROKHZAD, O.C., R. LANGER, Impact of nanotechnology on drug delivery, *ACS Nano*, 2009, **3**(1), 16–20, https://doi.org/10.1021/nn900002m.
12. FOROOZANDEH, P., A.A. AZIZ, Merging worlds of nanomaterials and biological environment: factors governing protein corona formation on nanoparticles and its biological consequences, *Nanoscale Research Letters*, 2015, **10**(1), 221, https://doi.org/10.1186/s11671-015-0922-3.
13. GANGWAR, R.K., G.B. TOMAR, V.A. DHUMALE, S. ZINJARDE, R.B. SHARMA, S. DATAR, Curcumin conjugated silica nanoparticles for improving bioavailability and its anticancer applications, *Journal of Agricultural and Food Chemistry*, 2013, **61**(40), 9632–9637, https://doi.org/10.1021/jf402894x.
14. GHISAIDOOBE, A.B.T., S.J. CHUNG, Intrinsic tryptophan fluorescence in the detection and analysis of proteins: A focus on Förster resonance energy transfer techniques, *International Journal of Molecular Sciences*, 2014, **15**(12), 22518–22538, https://doi.org/10.3390/ijms151222518.
15. GUPTA, S.C., S. PRASAD, J.H. KIM, S. PATCHVA, L.J. WEBB, I.K. PRIYADARSINIC B.B. AGGARWAL, Multitargeting by curcumin as revealed by molecular interaction studies, *Natural Product Reports*, 2011, **28**(12), 1937–1955, https://doi.org/10.1039/c1np00051a.
16. HAISS, W., N.T.K. THANH, J. AVEYARD, D.G. FERNIG, Determination of size and concentration of gold nanoparticles from UV-vis spectra, *Analytical Chemistry*, 2007, **79**(11), 4215–4221, https://doi.org/10.1021/ac0702084.
17. HAO, C., GUOQING XU, T. WANG, Z. LV, K. ZHU, B. LI, S. CHEN R. SUN, The mechanism of the interaction between curcumin and bovine serum albumin using fluorescence spectrum, *Russian Journal of Physical Chemistry B*, 2017, **11**(1), 140–145, https://doi.org/10.1134/S1990793117010043.
18. HOSSEN, M.N., C.K. ELECHALAWAR, V. SJOELUND, K. MOORE, R. MANNEL, R. BHATTACHARYA, P. MUKHERJEE, Experimental conditions influence the formation and composition of the corona around gold nanoparticles, *Cancer Nanotechnology*, 2021, **12**(1), https://doi.org/10.1186/s12645-020-00071-7.
19. HUGHES, T.J., P.L.A. POPELIER, Where does charge reside in amino acids? The effect of side-chain protonation state on the atomic charges of Asp, Glu, Lys, His and Arg, *Computational and Theoretical Chemistry*, 2015, **1053**, 298–304, https://doi.org/10.1016/j.comptc.2014.07.020.

20. JAISWAL, V.D., P.M. DONGRE, Biophysical interactions between silver nanoparticle-albumin interface and curcumin, *Journal of Pharmaceutical Analysis*, 2020, **10**(2), 164–177, https://doi.org/10.1016/j.jpha.2020.02.004.
21. JAISWAL, V.D., D.S. PANGAM, P.M. DONGRE, Biophysical study of cisplatin loaded albumin-gold nanoparticle and its interaction with glycans of gp60 receptor, *International Journal of Biological Macromolecules*, 2023, **231**, 123368, https://www.sciencedirect.com/science/article/abs/pii/S0141813023002544?via%3Dihub, [accessed 2026 Mar 2], https://doi.org/10.1016/j.ijbiomac.2023.123368.
22. EL KADI, N.N., TAULIER, J.Y. LE HUÉROU, I. NWIGWE, P.C. KAHN, M. WAKS, Unfolding and refolding of bovine serum albumin at acid pH: Ultrasound and structural studies, *Biophysical Journal*, 2006, **91**(9), 3397–3404, https://doi.org/10.1529/biophysj.106.088963.
23. KARNWAL, A., R.S.K. SACHAN, I. DEVGON, J. DEVGON, G. PANT, M. PANCHPURI, A. AHMAD, M.B. ALSHAMMARI, K. HOSSAIN G. KUMAR, Gold nanoparticles in nanobiotechnology: From synthesis to biosensing applications, *ACS Omega*, 2024, **9**(28), 29966–29982, https://doi.org/10.1021/acsomega.3c10352.
24. KOPAC, T., Protein corona, understanding the nanoparticle–protein interactions and future perspectives: A critical review, *International Journal of Biological Macromolecules*, 2021, 169, 290–301, https://www.sciencedirect.com/science/article/abs/pii/S0141813020352764?via%3Dihub, [accessed 2026 Mar 2], https://doi.org/10.1016/j.ijbiomac.2020.12.108.
25. LAKOWICZ, J.R., *Principles of Fluorescence Spectroscopy*, 3rd ed., Springer, 2006.
26. LAKSHMIKANTH, G.S., G. KRISHNAMOORTHY, Solvent-exposed trytophans probe the dynamics at protein surfaces, *Biophysical Journal*, 1999, **77**(2), 1100–1106, https://doi.org/10.1016/S0006-3495(99)76960-2.
27. LESNIAK, A. F. FENAROLI, M.P. MONOPOLI, C. ÅBERG, K.A. DAWSON, A. SALVATI, Effects of the presence or absence of a protein corona on silica nanoparticle uptake and impact on cells, *ACS Nano*, 2012, **6**(7), 5845–5857, https://doi.org/10.1021/nn300223w.
28. LI, D.D., X. GU, V. TIMCHENKO, Q.N. CHAN, A.C.Y. YUEN, G.H. YEOH, Study of morphology and optical properties of gold nanoparticle aggregates under different pH conditions, *Langmuir*, 2018, 34(35), 10340–10352, https://doi.org/10.1021/acs.langmuir.8b01457.
29. LI, X., K. NAN, L. LI, Z. ZHANG, H. CHEN, In vivo evaluation of curcumin nanoformulation loaded methoxy poly(ethylene glycol)-graft-chitosan composite film for wound healing application, *Carbohydrate Polymers*, 2012, **88**(1), 84–90, https://doi.org/10.1016/j.carbpol.2011.11.068.
30. LINK, S., M.A. EL-SAYED, Spectral properties and relaxation dynamics of surface plasmon electronic oscillations in gold and silver nanodots and nanorods, *Journal of Physical Chemistry B*, 1999, **103**(40), 8410–8426, https://doi.org/10.1021/jp9917648.
31. LÓPEZ-LÁZARO, M., Anticancer and carcinogenic properties of curcumin: considerations for its clinical development as a cancer chemopreventive and chemotherapeutic agent, *Molecular nutrition & food research*, 2008, **52** Suppl 1, S103–127, https://doi.org/10.1002/mnfr.200700238
32. LYNCH, I., KA. DAWSON, Protein-nanoparticle interactions, *Nano Today*, 2008, **3**(1–2), 40–47, https://www.sciencedirect.com/science/article/abs/pii/S1748013208700148, [accessed 2026 Mar 2], https://doi.org/10.1016/S1748-0132(08)70014-8.
33. MARIAM, J., P.M. DONGRE, D.C. KOTHARI, Study of interaction of silver nanoparticles with bovine serum albumin using fluorescence spectroscopy, *Journal of Fluorescence*, 2011, **21**(6), 2193–2199, https://doi.org/10.1007/s10895-011-0922-3.
34. MARIAM, J., S. SIVAKAMI, P.M. DONGRE, Elucidation of structural and functional properties of albumin bound to gold nanoparticles, *Journal Of Biomolecular Structure & Dynamics*, 2017, **35**(2), 368–379, https://doi.org/10.1080/07391102.2016.1144223.

35. Mohammadi, F., A.-K. Bordbar, A. Divsalar, K. Mohammadi, A.A. Saboury, Analysis of binding interaction of curcumin and diacetylcurcumin with human and bovine serum albumin using fluorescence and circular dichroism spectroscopy, *The Protein Journal*, 2009, **28**(3–4), 189–196, https://doi.org/10.1007/s10930-009-9184-1.
36. MONOPOLI, M.P., D. WALCZYK, A. CAMPBELL, G. ELIA, I. LYNCH, F. BALDELLI BOMBELLI, K.A. DAWSON, Physical-chemical aspects of protein corona: relevance to *in vitro* and *in vivo* biological impacts of nanoparticles, *Journal of the American Chemical Society*, 2011,133(8), 2525–2534, https://doi.org/10.1021/ja107583h.
37. MOUSTAPHA, A., P.A. PÉRÉTOUT, N.E. RAINEY, F. SUREAU, M. GEZE, J.-M. PETIT, E. DEWAILLY, C. SLOMIANNY, P.X. PETIT, Curcumin induces crosstalk between autophagy and apoptosis mediated by calcium release from the endoplasmic reticulum, lysosomal destabilization and mitochondrial events, *Cell Death Discovery*, 2015, **1**(1), Article number: 15017, https://doi.org/10.1038/cddiscovery.2015.17.
38. PEER, D., J.M. KARP, S. HONG, O.C. FAROKHZAD, R. MARGALIT, R. LANGER, Nanocarriers as an emerging platform for cancer therapy, *Nature Nanotechnology*, 2007, **2**(12), 751–760, https://doi.org/10.1038/nnano.2007.387.
39. PETERS, T., *All About Albumin: Biochemistry, Genetics, and Medical Applications*, Academic Press, 1996.
40. PIGNATARO, M.F., M.G. HERRERA, V.I. DODERO, Evaluation of peptide/protein self-assembly and aggregation by spectroscopic methods, *Molecules*, 2020, **25**(20), https://doi.org/10.3390/molecules25204854.
41. PRAMANIK, S., P. BANERJEE, A. SARKAR, S.C. BHATTACHARYA Size-dependent interaction of gold nanoparticles with transport protein: A spectroscopic study, *Journal of Luminescence*, 2008, **128**(12),1969–1974, https://www.sciencedirect.com/science/article/abs/pii/S0022231308001920 [accessed 2026 Mar 2], https://doi.org/10.1016/j.jlumin.2008.06.008.
42. RESENDE, L.F.T. DE-., *et al*., Revisiting the conformational transition model for the pH dependence of BSA structure using photoluminescence, circular dichroism, and ellipsometric Raman spectroscopy, *International Journal of Biological Macromolecules*, 2024, 259, 129142. https://www.sciencedirect.com/science/article/abs/pii/S0141813023060415 [accessed 2026 Mar 3], https://doi.org/10.1016/j.ijbiomac.2023.129142.
43. RÖCKER, C., M. PÖTZL, F. ZHANG, W.J. PARAK G.U. NIENHAUS, A quantitative fluorescence study of protein monolayer formation on colloidal nanoparticles, *Nature Nanotechnology*, 2009, **4**(9), 577–580, https://doi.org/10.1038/nnano.2009.195.
44. SWIETACH, P., R.D. VAUGHAN-JONES, A.L. HARRIS, A. HULIKOVA The chemistry, physiology and pathology of pH in cancer, *Philosophical Transactions of the Royal Society B: Biological Sciences*, 2014, **369**(1638), 577–580, https://doi.org/10.1098/rstb.2013.0099.
45. VALLIANOU, N.G., A. EVANGELOPOULOS, N. SCHIZAS, C. KAZAZIS Potential anticancer properties and mechanisms of action of curcumin, *Anticancer research*, 2015, **35**(2), 645–651.
46. WALKEY, C.D., W.C.W. CHAN, Understanding and controlling the interaction of nanomaterials with proteins in a physiological environment, *Chem. Soc. Rev*, 2012, **41**(7), 2780–2799, https://doi.org/10.1039/C1CS15233E.
47. WANG, Y., Y. NI, Combination of UV–vis spectroscopy and chemometrics to understand protein-nanomaterial conjugate: A case study on human serum albumin and gold nanoparticles, *Talanta*, 2014 **119**, 320–330, https://www.sciencedirect.com/science/article/abs/pii/S003991401300903X [accessed 2026 Mar 2], https://doi.org/10.1016/j.talanta.2013.11.026.
48. WEBB, B.A., M. CHIMENTI, M.P. JACOBSON, D.L. BARBER, Dysregulated pH: a perfect storm for cancer progression, *Nature Reviews. Cancer*, 2011, **11**(9), 671–677, https://doi.org/10.1038/nrc3110.

49. WÏNIEWSKA, M., K. SZEWCZUK-KARPISZ, D. STERNIK Adsorption and thermal properties of the bovine serum albumin-silicon dioxide system, *Journal of Thermal Analysis and Calorimetry*, 2015, **120**(2), 1355–1364, https://doi.org/10.1007/s10973-014-4300-7.
50. YU, X., Y. ZHANG, C. CHEN, Q. YAO, M. LI, Targeted drug delivery in pancreatic cancer, *Biochimica et Biophysica Acta - Reviews on Cancer*, 2010, **1805**(1), 97–104, https://doi.org/10.1016/j.bbcan.2009.10.001.
51. ZHAI, K., A. BROCKMÜLLER, P. KUBATKA, M. SHAKIBAEI, D. BÜSSELBERG, Curcumin's beneficial effects on neuroblastoma: Mechanisms, challenges, and potential solutions, *Biomolecules*, 2020, **10**(11), 1–28, https://doi.org/10.3390/biom10111469.